arXiv:1512.03753v2 [cond-mat.mes-hall] 13 May 2016

Macroscopic degeneracy of zero-mode rotating surface states in 3D Dirac and Weyl semimetals under radiation

José González and Rafael A. Molina
Instituto de Estructura de la Materia, IEM-CSIC, Serrano 123, Madrid 28006, Spain

We investigate the development of novel surface states when 3D Dirac or Weyl semimetals are placed under circularly polarized electromagnetic radiation. We find that the hybridization between inverted Floquet bands opens in general a gap, which closes at so-called exceptional points found for complex values of the momentum. This corresponds to the appearance of midgap surface states in the form of evanescent waves decaying from the surface exposed to the radiation. We observe a phenomenon reminiscent of Landau quantization by which the midgap surface states get a large degeneracy proportional to the radiation flux traversing the surface of the semimetal. We show that all these surface states carry angular current, leading to an angular modulation of their charge that rotates with the same frequency of the radiation, which should manifest in the observation of a macroscopic chiral current in the irradiated surface.

Introduction.— In recent years we have witnessed the discovery of several types of materials characterized by having electron quasiparticles with linear momentum dispersion. Graphene was certainly the first of those materials[1], but afterwards we learned about the topological insulators[2, 3], to end up more recently with the investigation of 3D semimetals whose low-energy excitations behave as Dirac[4–6] or Weyl fermions[7, 8].

These materials have attracted a lot of attention for their potential to develop a new type of electronic transport without dissipation. The key idea is that of topological protection, which has its precedent in the edge states of the quantum Hall effect. The surface states in the novel materials may also have a well-defined chirality, protecting them against backscattering. Both properties are fundamental for revolutionary applications in spintronics and fault-tolerant quantum computation [2, 3].

In this search, the interaction between light and matter can play an important role, since the electromagnetic radiation may be a versatile resource to change and control topological states of matter. In 2D semimetals, it can open a gap in the bulk, leading to chiral currents at the boundary of the electron system[9–18], as observed on the surface of 3D topological insulators[19]. The effect of the radiation has been also investigated in the case of 3D Dirac and Weyl semimetals, focusing on bulk properties[20–22].

In this paper, we investigate the development of novel surface states when a 3D Dirac or Weyl semimetal is placed under circularly polarized electromagnetic radiation. We will show that such states are intimately related to avoided crossings at the gap that opens up from the hybridization of inverted Floquet bands, as represented in Fig. 1. The gap closes at so-called exceptional points (EPs) [23, 24], which are celebrated in the context of non-Hermitian Hamiltonians and appear here for complex values of the momentum describing the evanescence into the 3D semimetal. The stability of the novel surface states is then guaranteed by a new mechanism of topological protection, relying on the fact that each EP comes as a branch point in the spectrum which cannot be removed by small perturbations.

The genuine feature of the novel surface states is that they all carry a significant angular current, with the same chirality of the photon polarization and the frequency of the radiation. Such states may prove especially useful in the current drive towards increasing the frequency limits of electronic devices [25].

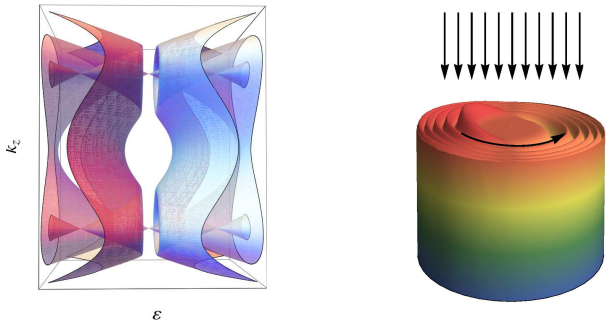

FIG. 1. Left: Schematic representation of the first Floquet bands with quasi-energy ϵ and $\epsilon \pm \hbar\Omega$ (Ω being the radiation frequency) for a model of 3D semimetal with two nodes along the momentum axis k_z (red color denotes positive energy while light blue denotes negative energy, the direction transverse to k_z represents additional components of the momentum). Right: Geometry of 3D semimetal with the surface exposed to the radiation where the evanescent states appear.

Model and Floquet theory.— A low-energy Hamiltonian for a 3D Dirac semimetal around the Brillouin zone center, considering terms up to quadratic order in the quasimomentum $\mathbf{k}$, can be written as [26, 27].

$$H = \epsilon_0(\mathbf{k})\mathbb{I} + M(\mathbf{k})\sigma_z + \hbar v(\zeta k_x\sigma_x - k_y\sigma_y) \quad (1)$$

$$\epsilon_0(\mathbf{k}) = c_0 + c_1k_z^2 + c_2(k_x^2 + k_y^2) \quad (2)$$

$$M(\mathbf{k}) = m_0 - m_1k_z^2 - m_2(k_x^2 + k_y^2), \quad (3)$$

where $\mathbb{I}$ is the 2×2 identity matrix, σ_i, $i = x, y, z$, are the Pauli matrices, and $\zeta = \pm 1$ sets the chirality in the

Dirac cones. The solution of the eigenvalue problem is

$$E_\pm = \epsilon_0(\mathbf{k}) \pm \sqrt{M(\mathbf{k})^2 + \hbar^2 v^2 (k_x^2 + k_y^2)}. \qquad (4)$$

With the parameters $m_0, m_1, m_2 < 0$ to reproduce band inversion, the spectrum shows Dirac crossings at $\mathbf{k}_c = (0, 0, \pm\sqrt{m_0/m_1})$. Ignoring the part proportional to the unit matrix $\epsilon_0(\mathbf{k})$, we can expand the Hamiltonian linearly around each Dirac point to obtain a model for 3D massless Dirac fermions with anisotropic linear dispersion $E(\mathbf{k}) = \pm\sqrt{\hbar^2 v^2 (k_x^2 + k_y^2) + 4 m_0 m_1 (k_z - k_{c,z})^2}$.

Consider illumination by circularly polarized off-resonant light of frequency Ω and field amplitude $\mathcal{F}$. In the case of polarization in the $x-y$ plane, light produces the vector potential in the dipolar approximation $\mathcal{A}(t) = \mathcal{A}(\eta \sin\Omega t, \cos\Omega t, 0)$, where $\eta = \pm 1$ for right and left circularly polarized beams, respectively, and $\mathcal{A} = \mathcal{F}/\Omega$. We make the Peierls substitution $\mathbf{k} \to \mathbf{k} + \mathcal{A}(t)$ and use Floquet theory in order to compute the band structure in the presence of the radiation field[28]. Solutions of the time-dependent Schrödinger equation in the case of time-periodic Hamiltonians have the form $|\Psi(t)\rangle = e^{-i\epsilon t/\hbar} |\Phi(t)\rangle$, with a conserved quantity, the quasi-energy ϵ, playing a similar role to the energy in the time-independent Schödinger equation. The Floquet states $|\Phi(t)\rangle$ are periodic in time with the same period as the Hamiltonian and they can be developed in Fourier series, $|\Phi(t)\rangle = \sum_m e^{-im\Omega t} |u_\alpha^m\rangle$. This transforms the time-dependent Schrödinger equation into

$$\sum_n H^{mn} |u_\alpha^n\rangle = (\epsilon_\alpha + m\hbar\Omega) |u_\alpha^m\rangle , \qquad (5)$$

where the Floquet Hamiltonian matrix elements are given by $H^{mn} = \frac{1}{T}\int_0^T dt H(t) e^{i(m-n)\Omega t}$, $T = 2\pi/\Omega$ being the period of the time-dependent Hamiltonian[28].

As a relevant example, we perform calculations in an infinite wire in the z direction with a finite square section in the $x-y$ plane. Using the Floquet formalism, we calculate the band structure as a function of k_z discretizing the model Hamiltonian with a standard tight-binding regularization including the Floquet subbands. Results with parameters of the model in the topological Dirac semimetal regime are shown in Fig. 2, where we compare the energy of the bulk bands (left) with the quasi-energy of the bands in the wire (right) as a function of k_z. The structure of the bands wrapping up in the Floquet-Brillouin zone is very apparent. In the middle of the Floquet-Brillouin zone at $\epsilon = 0$, a gap opens between states with Floquet modes $n = -1$ (red) and $n = 1$ (blue), the hybridization being a second order effect leading to a quite small gap, proportional to $\mathcal{A}^2$. The much bigger gap (proportional to $\mathcal{A}$) between modes $n = 0$ (green) and $n = 1$ is in one of the edges of the Floquet-Brillouin zone at $\epsilon = \hbar\Omega/2$, with a mirror structure (not shown) at $\epsilon = -\hbar\Omega/2$ between modes $n = 0$ and $n = -1$.

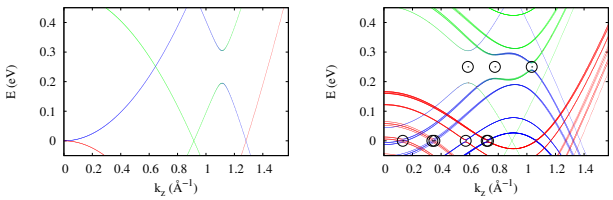

FIG. 2. Band structure for model parameters $c_0 = c_1 = c_2 = 0.0$, $m_0 = -0.5$ eV, $m_1 = -0.605$ eV Å^2, $m_2 = -1.0$ eV Å^2, $\hbar v = 1.1$ eV Å, $\hbar\Omega = 0.5$ eV, $\mathcal{A} = 0.05$ Å^{-1}, in the bulk (left panel) and for a wire of section $S = 150 \times 150$ Å^2 in the $x-y$ plane (right panel). The position of the Dirac cone at zero field is $k_{c,z} = \sqrt{m_0/m_1} = 0.909$ Å^{-1}. The color represents the predominant Floquet mode of the particular state in a RGB coding where the intensity of each mode is mapped to the intensity of each fundamental color, $n = -1, 0, 1$ correspond to red, green and blue, respectively. The position of the evanescent waves obtained as strictly real solutions of the eigenvalue problem after including an imaginary part in k_z of $\mathrm{Im}(k_z) = 0.01$ Å^{-1} is shown with black circles with a dot. A few high-energy bands with $n = -1$ index not affecting the avoided crossing structures have been erased for clarity of presentation.

In order to explore the possibility of evanescent states in the z direction, we solve the Schrödinger equation in the same geometry but including a finite imaginary part in k_z. The Hamiltonian becomes then non-Hermitian and the eigenenergies acquire a finite imaginary part. These are obviously non-physical solutions of the problem. However, non-Hermitian Hamiltonians may have eigenenergies that are strictly real, in the form of EPs [23, 24]. These correspond to physical evanescent solutions with the imaginary part of the momentum giving the decay length of a wave in a semi-infinite geometry. The black circles in Fig. 2 mark the presence of the evanescent states in the gaps induced by the radiation. Not all the avoided crossings present evanescent states, that depends on the properties of the actual bands involved. However, the number of avoided crossings is proportional to $\mathcal{A}$ and to the area of the section of the wire. This may imply in general a large degeneracy of evanescent states, whose origin is clarified in the continuum limit discussed in what follows.

Quantization and localization of zero-mode surface states.— In order to unveil the properties of the novel surface states, we focus now on the low-energy physics around any of the nodes of the Hamiltonian (1), taking moreover the projection for a given chirality ζ. This amounts to linearize $M(\mathbf{k})$ about the node at $\mathbf{k} = \mathbf{k}_c$, which leads in real space to the Hamiltonian for a single Weyl quasiparticle

$$\begin{aligned} H_W = &-i\hbar(v\sigma_x\partial_x + v\sigma_y\partial_y + v_z\sigma_z\partial_z) \\ &+\hbar v\mathcal{A}\left(\sigma_x\cos(\Omega t) + \sigma_y\sin(\Omega t)\right) \end{aligned} \qquad (6)$$

with a velocity $v_z \neq v$ along the z-axis[29].

H_W can be translated into a time-independent Hamiltonian after applying the unitary transformation $U = e^{-iJ_z\Omega t/\hbar}$, with the projection of the total angular momentum $J_z = -i\hbar x\partial_y + i\hbar y\partial_x + \hbar\sigma_z/2$ [30]. This leads to the transformed Hamiltonian

$$\begin{aligned}\widetilde{H}_W &= U^\dagger H_W U - i\hbar U^\dagger \partial_t U \\ &= -i\hbar(v\sigma_x\partial_x + v\sigma_y\partial_y + v_z\sigma_z\partial_z) - \Omega J_z + \hbar v\mathcal{A}\sigma_x \quad (7)\end{aligned}$$

Each eigenvector χ of (7) corresponds then to a solution $\Psi(t)$ of the original time-dependent Schrödinger equation, given by $\Psi(t) = e^{-iJ_z\Omega t/\hbar}e^{-i\varepsilon t/\hbar}\chi$ (ε being the eigenvalue of (7)). This shows that the eigenvalues j_z of the projection J_z can be used in this approach to label the different side bands arising from the irradiation.

After applying the gauge transformation $P = \exp(-i\mathcal{A}x)$ to (7), the Hamiltonian becomes (in polar coordinates r, θ and with $\sigma_\pm = (\sigma_x \pm i\sigma_y)/2$)

$$\begin{aligned}\widetilde{H}'_W = &-i\hbar v\sum_{s=\pm} e^{-si\theta}\left(\partial_r - si\frac{1}{r}\partial_\theta\right)\sigma_s \\ &-i\hbar v_z\sigma_z\partial_z - \hbar\Omega\left(-i\partial_\theta + \frac{\sigma_z}{2}\right) - \hbar\Omega\mathcal{A}r\sin(\theta) \quad (8)\end{aligned}$$

The last term in (8) is responsible for the coupling between states with different angular momenta j_z. Then, the avoided crossing of the bands with $j_z = \pm\hbar/2$ gives rise to a gap around zero energy in the spectrum of (8). This point corresponds actually to a quasi-energy $\epsilon = \hbar\Omega/2$ in the conventional Floquet approach, since U has the effect of shifting the energy of the side bands in the present approach by half-integer multiples of $\hbar\Omega$.

The development of the gap can be captured (for not too large amplitude $\mathcal{A}$) by solving in the space spanned by a linear combination of spinors with projection of the total angular momentum $j_z = \pm\hbar/2$,

$$\chi = \begin{pmatrix}\phi_1(r)\\ e^{i\theta}\phi_2(r)\end{pmatrix}e^{ik_z z} + \begin{pmatrix}e^{-i\theta}\phi_3(r)\\ \phi_4(r)\end{pmatrix}e^{ik_z z} \quad (9)$$

We have considered specifically a cylindrical geometry with the section at $z = 0$ exposed to the radiation, as represented in Fig. 1 [31]. A typical shape of the gap is shown in Fig. 3(a), where we see that it has several oscillations before recovering the linear dispersion of the original cones beyond a certain k_z. This is indeed the generic behavior, with an increasing number of oscillations as the radius R of the cylinder grows.

The origin of the oscillations in the gap is clarified by noting that they arise from the existence of EPs in the spectrum of the Hamiltonian (8), corresponding to values of k_z inside the complex plane where the gap closes. Around each oscillation of the gap, the lowest eigenvalue ε behaves as a function of complex k_z as $\varepsilon \sim \sqrt{k_i - k_z}\sqrt{\overline{k}_i - k_z}$, with EPs at complex conjugate momenta $k_i, \overline{k}_i$ [28]. Evanescent states with $\mathrm{Im}(\varepsilon) = 0$ exist then in the segment $|\mathrm{Im}(k_z)| \leq |\mathrm{Im}(k_i)|$, for each

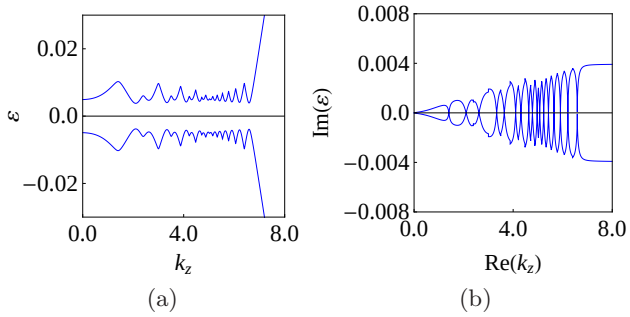

FIG. 3. (a) Plot of the gap of the Hamiltonian (8) (in eV) as a function of real k_z (measured in units of the inverse of the typical microscopic length scale a in the material) for $\hbar v/a = 1.1$ eV, $\hbar\Omega = 0.5$ eV, $\mathcal{A} = 0.005\, a^{-1}$, and radius $R = 200a$ of the cylindrical geometry considered in the text. (b) Imaginary part of the lowest eigenvalue of the Hamiltonian (8) (in eV) as a function of $\mathrm{Re}(k_z)$, for complex momenta with $\mathrm{Im}(k_z) = 0.08\, a^{-1}$ and the same parameters as in (a).

pair $k_i, \overline{k}_i$. We have represented for instance in Fig. 3(b) the behavior of the imaginary part of the lowest eigenvalue, when $\mathrm{Im}(k_z) \neq 0$, as a function of the real part of k_z. We observe the recurrent development of complex momenta at which the eigenvalue becomes purely real, leading to a set of evanescent eigenstates in perfect correspondence with the minima of the gap in Fig. 3(a).

We find then that the evanescent states are preserved by a mechanism of topological protection, as the branch cuts cannot be undone in the complex plane unless the branch points coalesce in pairs. It can be seen that the imaginary part of the EPs has a very smooth dependence on the frequency Ω, while it grows linearly with the amplitude $\mathcal{A}$ [32]. The number of zero-mode evanescent states may be actually characterized from the number of branch points that the lowest band $\varepsilon(k_z)$ has in the complex plane.

It can be checked that the number of EPs increases as the radius R grows, leading to a definite pattern of quantization in the surface of our geometry. It can be seen that the order of each zero in the plot of Fig. 3(b) (from right to left) gives also the extent of the localization that the corresponding evanescent wave has in the radial direction, as illustrated in Fig. 4. The peak in the probability distribution shifts to lower values of r as $\mathrm{Re}(k_z)$ decreases, reaching eventually the innermost region of the surface. The number of evanescent states, besides growing linearly with the frequency Ω and the amplitude $\mathcal{A}$, becomes actually proportional to the area of the irradiated surface, at a rate of roughly one state per $(100a)^2$ (for $\hbar\Omega = 0.1$ eV, $\mathcal{A} = 0.01\, a^{-1}$, a being a typical microscopic length scale in the material).

Furthermore, the midgap evanescent states evolve in time with a rotation of their charge along the angular variable θ. This can be shown by computing the an-

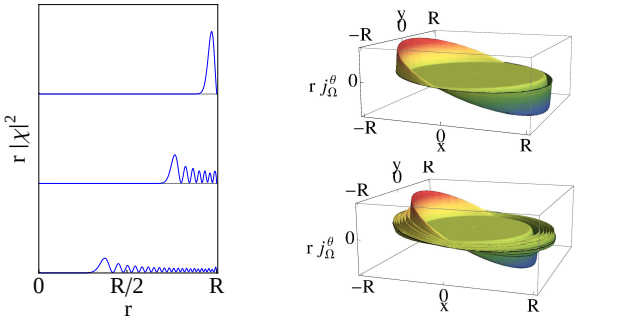

FIG. 4. Left: Probability distribution $r|\chi|^2$ along the radial direction for evanescent states corresponding to three decreasing values of $\mathrm{Re}(k_z)$ with $\mathrm{Im}(\varepsilon)=0$ (starting with the outermost evanescent state) for the same parameters as in Fig. 3 and $R=400a$. Right: Time-dependent angular current rj^θ_Ω for the states in the upper part (top) and the middle part (bottom) of the left panel, represented for fixed time $t=0$ at the irradiated surface of the cylindrical geometry.

gular component j^θ of the probability current for the Hamiltonian (6). This current has a static contribution, $j^\theta_{\rm static}=-i(v/r)(\phi_1^*\phi_2+\phi_3^*\phi_4)+$h.c., which leads to a very small intensity when integrated over the radial direction, as a consequence of the tendency of the two contributions from $j_z=\pm\hbar/2$ states to cancel each other[28]. For $\hbar\Omega=0.5$ eV and $\mathcal{A}=0.005\,a^{-1}$, we get for instance values of the intensity $\int dr\, rj^\theta_{\rm static}$ between $\sim 10^{-5}v/a$ and $\sim 10^{-4}v/a$, when computing for evanescent states from the outermost to the innermost region of the surface. However, there is also a non-negligible time-dependent contribution to j^θ [28], given by

$$j^\theta_\Omega=-i(v/r)(\phi_1^*\phi_4 e^{-i(\theta-\Omega t)}+\phi_3^*\phi_2 e^{i(\theta-\Omega t)})+\text{h.c.} \quad (10)$$

which has a periodic dependence on $\theta-\Omega t$ as shown in Fig. 4 [33]. The intensity corresponding to j^θ_Ω has maxima (in the angular variable) which turn out to be in general about two orders of magnitude above the intensity obtained from $j^\theta_{\rm static}$, for every evanescent state[28].

When introduced in the continuity equation, the form of j^θ_Ω implies that the charge of each state must have a periodic modulation in the angular variable, and that it must rotate with frequency Ω along the concentric rings where each evanescent state is confined[28]. From a practical point of view, this leads to the formation of rotating dipoles on the surface of the system, whose movement can be controlled by tuning the parameters of the radiation.

While we have referred here to the hybridization of states with $j_z=\pm\hbar/2$, the coupling of side bands with higher values of J_z results in surface states with similar properties of localization and time evolution[28]. It can be seen in particular that the hybridization of side bands with values of j_z differing by $2\hbar$ leads also to evanescent states, which correspond in that case to the EPs found at $\epsilon=0$ in the preceding section.

Conclusion.— An important practical consideration in this study is that the infrared radiation may penetrate sufficiently deep into the 3D semimetals, given the limited screening in these materials. The penetration length l can be estimated as the inverse of the absorption coefficient α, which is expressed in terms of the dielectric function $\epsilon(\Omega)$ as $\alpha=2\Omega\mathrm{Im}\sqrt{\epsilon(\Omega)}/c$. We find for instance that $l\sim 1\ \mu m$ in the near-infrared ($\Omega\sim 100$ THz)[28], which is a large enough distance to afford the development of the evanescent states.

The magnitude of the component j^θ_Ω of the current offers good perspectives to observe experimentally the novel surface states. In our cylindrical geometry, the intensity of the current across the radial direction, $I=e\int dr\, rj^\theta_\Omega$, gets maxima (in the angular variable) that range between $\sim 10^{-1}\ \mu A$ and $\sim 1\ \mu A$, for individual states taken from the outermost to the innermost region in the top surface. The total intensity could be enhanced by a large additional factor, in a device able to measure the contribution of a significant part of the surface states.

A suitable experimental setup (i.e. two electrodes on top of the surface of the semimetal) may be able to convert the rotation of the charge in the surface states into an electrical current, if the device is made to work as a rectenna. This may benefit from recent developments which make possible to rectify currents oscillating even at the frequency of visible light[34]. In our case, it may greatly help the fact that the rotation of all the surface states is synchronized with that of the radiation fields, making easier the observation of the macroscopic chiral current that may develop at the irradiated surface.

We acknowledge financial support from MICINN (Spain) through grant No. FIS2011-23713 and MINECO (Spain) through grants No. FIS2012-34479 and FIS2014-57432-P.

[1] K. S. Novoselov, A. K. Geim, S. V. Morozov, D. Jiang, Y. Zhang, S. V. Dubonos, I. V. Grigorieva, and A. A. Firsov, Electric field effect in atomically thin carbon films, Science **306**, 666 (2004).
[2] M. Z. Hasan and C. L. Kane, Topological insulators, Rev. Mod. Phys. **82**, 3045 (2010).
[3] X.-L. Qi and S.-C. Zhang, Topological insulators and superconductors, Rev. Mod. Phys. **83**, 1057 (2011).
[4] Z. K. Liu, B. Zhou, Y. Zhang, Z. J. Wang, H. M. Weng, D. Prabhakaran, S.-K. Mo, Z. X. Shen, Z. Fang, X. Dai, Z. Hussain and Y. L. Chen, Discovery of a Three-Dimensional Topological Dirac Semimetal, Na_3Bi, Science **343**, 864 (2014).
[5] M. Neupane, S. Xu, R. Sankar, N. Alidoust, G. Bian, C. Liu, I. Belopolski, T.-R. Chang, H.-T. Jeng, H. Lin, A. Bansil, F. Chou and M. Z. Hasan, Observation of a three-dimensional topological Dirac semimetal phase in high-mobility Cd_3As_2, Nature Commun. **5**, 3786 (2014).
[6] S. Borisenko, Q. Gibson, D. Evtushinsky, V. Zabolotnyy,

B. Büchner and R. J. Cava, Experimental realization of a three-dimensional Dirac semimetal, Phys. Rev. Lett. **113**, 027603 (2014).
[7] S.-Y. Xu, I. Belopolski, N. Alidoust, M. Neupane, G. Bian, C. Zhang, R. Sankar, G. Chang, Z. Yuan, C.-C. Lee, S.-M. Huang, H. Zheng, J. Ma, D. S. Sanchez, B. Wang, A. Bansil, F. Chou, P. P. Shibayev, H. Lin, S. Jia, and M. Z. Hasan, Discovery of a Weyl fermion semimetal and topological Fermi arcs, Science **349**, 613 (2015).
[8] B. Q. Lv, H. M. Weng, B. B. Fu, X. P. Wang, H. Miao, J. Ma, P. Richard, X. C. Huang, L. X. Zhao, G. F. Chen, Z. Fang, X. Dai, T. Qian, and H. Ding, Experimental discovery of Weyl semimetal TaAs, Phys. Rev. X **5**, 031013 (2015).
[9] T. Oka and H. Aoki, Photovoltaic Hall effect in graphene, Phys. Rev. B **79**, 081406 (2009).
[10] N. H. Lindner, G. Refael, and V. Galitski, Floquet topological insulators, Nature Phys. **7**, 490 (2011).
[11] J.-I. Inoue and A. Tanaka, Photoinduced transition between conventional and topological insulators in two-dimensional electronic systems, Phys. Rev. Lett. **105**, 017401 (2010).
[12] T. Kitagawa, E. Berg, M. Rudner, and E. Demler, Topological characterization of periodically driven quantum systems, Phys. Rev. B **82**, 235114 (2010).
[13] T. Kitagawa, T. Oka, A. Brataas, L. Fu, and E. Demler, Transport properties of nonequilibrium systems under the application of light: Photoinduced quantum Hall insulators without Landau levels, Phys. Rev. B **84**, 235108 (2011).
[14] Z. Gu, H. A. Fertig, D. P. Arovas, and A. Auerbach, Floquet spectrum and transport through an irradiated graphene ribbon, Phys. Rev. Lett. **107**, 216601 (2011).
[15] H.L. Calvo, H.M. Pastawski, S. Roche, L.E.F. Foa Torres, Tuning laser-induced band gaps in graphene, Appl. Phys. Lett. **98**, 232103 (2011).
[16] A. Gómez-León, G. Platero, Floquet-Bloch Theory and Topology in Periodically Driven Lattices, Phys. Rev. Lett. **110**, 200403 (2013).
[17] P.M. Perez-Piskunow, G. Usaj, C.A. Balseiro, L.E.F. Foa Torres, Floquet chiral edge states in graphene, Phys. Rev. B **89**, 121401(R) (2014).
[18] H.L. Calvo, L.E.F. Foa Toores, P.M. Perez-Piskiunow, C.A. Balseiro, G. Usaj, Floquet interface states in illuminated three dimensional topological insulators, Phys. Rev. B **91**, 241404(R) (2015).
[19] Y. H. Wang, H. Steinberg, P. Jarillo-Herrero, and N. Gedik, Observation of Floquet-Bloch states on the surface of a topological insulator, Science **342**, 453 (2013).
[20] R. Wang, B. Wang, R. Shen, L. Sheng, D. Y. Xing, Floquet Weyl semimetal induced by off-resonant light, Europhys. Lett. **105**, 17004 (2014).
[21] A. Narayan, Floquet dynamics in two-dimensional semi-Dirac semimetals and three-dimensional Dirac semimetals, Phys. Rev. B **91**, 205445 (2015).
[22] C.-K. Chan, P. A. Lee, K. S. Burch, J. H. Han, and Y. Ran, When chiral photons meet chiral fermions: photoinduced anomalous Hall effects in Weyl semimetals, Phys. Rev. Lett. **116**, 026805 (2016).
[23] M. V. Berry, Physics of nonhermitian degeneracies, Czech. J. Phys. **54**, 1039 (2004).
[24] W. D. Heiss, The physics of exceptional points, J. Phys. A: Math. Theor. **45**, 444016 (2012).
[25] F. Krausz, M.I. Stockman, Attosecond metrology: from electron capture to future signal processing, Nat. Photonics **8**, 205 (2014).
[26] Z. Wang, Y. Sun, X.-W. Chen, C. Franchini, G. Xu, H. Weng, X. Dai, Z. Fang, Dirac semimetal and topological phase transitions in A_3Bi (A=Na,K,Rb), Phys. Rev. B **85**, 195320 (2012).
[27] Z. Wang, H. Weng, Q. Wu, X. Dai, Z. Fang, Three-dimensional Dirac semimetal and quantum transport in Cd_3As_2, Phys. Rev. B **88**, 125427 (2013).
[28] See supplemental material.
[29] We set in what follows $v_z = 0.05v$, taking as a guide the relative magnitudes observed in real 3D semimetals.
[30] A. López, A. Scholz, B. Santos, and J. Schliemann, Photoinduced pseudospin effects in silicene beyond the off-resonant condition, Phys. Rev. B **91**, 125105 (2015).
[31] We note that, in the semi-infinite geometry, two modes with momenta k_z and $-k_z$ are to be superposed, in order to build each eigenstate vanishing at the top boundary of the cylinder.
[32] A typical magnitude of the imaginary part of the EPs is for instance $\mathrm{Im}(k_i) \sim 0.1\, a^{-1}$, for $\hbar\Omega = 0.5$ eV and $\mathcal{A} = 0.005\, a^{-1}$, where a stands for a typical microscopic length scale in the material.
[33] Our definition of the current in Eq. (10) (as well as that of $j^{\theta}_{\mathrm{static}}$) omits for simplicity its decay along the z-axis, which is inherited from the evanescence of the surface states.
[34] A. Sharma, V. Singh, T. L. Bougher, and B. A. Cola, A carbon nanotube optical rectenna, Nature Nanotech. **10**, 1027 (2015).

SUPPLEMENTAL MATERIAL

Penetration depth of the electromagnetic radiation in 3D Dirac and Weyl semimetals

We analyze here the penetration depth of the electromagnetic radiation in a 3D semimetal, focusing on absorption due to interband transitions between available electronic states. We start by noting that the refractive index n of the material can be expressed in terms of the dielectric function $\epsilon(\omega)$ as

$$n = \sqrt{\epsilon(\omega)} \tag{11}$$

According to this expression, n may get in general an imaginary part, which accounts for the absorption of the electromagnetic radiation by the electron system.

A measure of the exponential decay of the radiation energy in the material is given by the absorption coefficient α, from which the penetration length l can be estimated as $\sim 1/\alpha$. The absorption coefficient can be obtained from the refractive index as

$$\alpha(\omega) = (2/c)\,\omega\,\mathrm{Im}\,n(\omega) \tag{12}$$

In the 3D semimetals, the imaginary part of the dielectric function $\epsilon(\omega)$ has a smooth dependence on frequency, so that the leading dependence of α on ω is linear. More specifically, the dielectric function in a 3D Dirac semimetal with N Dirac points (or, equivalently, in a 3D Weyl semimetal with N pairs of Weyl points) is given at low energies by

$$\epsilon(\omega) = \frac{Ne^2}{6\pi^2\hbar v}\,\log\left(\frac{\Lambda}{|\omega|}\right) + i\frac{Ne^2}{12\pi\hbar v} \tag{13}$$

where Λ is a high-frequency cutoff (related to the high-energy cutoff in the linear electronic dispersion) and v is the Fermi velocity (assuming for simplicity that the dispersion is isotropic in all directions).

Taking typical parameters for known 3D semimetals and keeping $N \sim 1$, we get from Eq. (12) a penetration length $l \sim 100$ nm for visible light, and $l \sim 1\,\mu$m in the near-infrared (with $\omega = 100$ THz). This shows that the use of infrared radiation may become specially convenient, for the sake of observing the interaction between electromagnetic radiation and the 3D semimetal proposed in the main text.

High-frequency effective Hamiltonian for the 3D Dirac semimetal in the presence of circularly polarized radiation

Using the following equations

$$H^{mn} = \frac{1}{T}\int_0^T dt H(t) e^{i(m-n)\Omega t}, \tag{14}$$

we can compute the Floquet matrix elements of the model for a 3D Dirac semimetal. In our model the only non-zero matrix-elements are H_{nn}, $H_{+1} = H_{n+1n}$, $H_{-1} = H_{n-1n}$. The matrix elements $H_{+2} = H_{n+2n}$, $H_{-2} = H_{n-2n}$ are zero due to cancellations coming from the shape of the circularly polarized pulses. It is then, easy to see that the diagonal part of the Floquet Hamiltonian is:

$$H_{nn} = H + (n\hbar\Omega + c_2\mathcal{A}^2)\mathbb{I} - m_2\mathcal{A}^2\sigma_z, \tag{15}$$

This is equivalent to a renormalization of the c_0 and m_0 parameters in the Hamiltonian H, which become $c_0 + c_2\mathcal{A}^2$ and $m_0 - m_2\mathcal{A}^2$ respectively. The non-diagonal parts are

$$\begin{aligned} H_{+1} = {} & \frac{i}{2}\hbar v\mathcal{A}\eta\zeta\sigma_x - \frac{1}{2}\hbar v\mathcal{A}\sigma_y \\ & + [(c_2 - m_2\sigma_z)i\mathcal{A}\eta k_x + (c_2 - m_2\sigma_z)\mathcal{A}k_y]. \end{aligned} \tag{16}$$

$$\begin{aligned} H_{-1} = {} & -\frac{i}{2}\hbar v\mathcal{A}\eta\zeta\sigma_x - \frac{1}{2}\hbar v\mathcal{A}\sigma_y \\ & + [(m_2\sigma_z - c_2)i\mathcal{A}\eta k_x + (c_2 - m_2\sigma_z)\mathcal{A}k_y]. \end{aligned} \tag{17}$$

The effective high-frequency Hamiltonian when only one-photon processes are taken into account can be written as

$$H_{\rm eff} = H_{00} + \frac{[H_{-1}, H_{+1}]}{\hbar\Omega}. \tag{18}$$

For the model of a 3D Dirac semimetal used in the paper:

$$H_{\rm eff} = H_{00} - \eta\frac{\hbar v^2\mathcal{A}^2}{\Omega}\sigma_z - 2m_2\eta\frac{v\mathcal{A}^2}{\Omega}(k_x\sigma_x - k_y\sigma_y). \tag{19}$$

The terms proportional to σ_z change the effective mass terms so the new effective m_0 is

$$m_0^{\rm eff} = m_0 - m_2\mathcal{A}^2 - \eta\frac{\hbar v^2\mathcal{A}^2}{\Omega}. \tag{20}$$

The terms proportional to $\sigma_{x(y)}$ renormalize the parameter v

$$v^{\rm eff} = v - 2m_2\eta\frac{v\mathcal{A}^2}{\hbar\Omega}. \tag{21}$$

The Dirac crossing points are displaced decreasing or increasing the distance between them depending on the polarization of the external field η. Choosing the parameters of the external field wisely, we can switch the band inversion on or off by changing the sign of $m_0^{\rm eff}$. Although the high-frequency approximation fails to properly describe the details of the band structure except for very high-frequency fields or for very small amplitudes, it gives us good estimates of the parameters needed for switching the band inversion. Examples of band structures in the first Floquet-Brillouin zone (quasi-energy $\epsilon \in [-\hbar\Omega/2, \hbar\Omega/2]$) are shown in Fig. 5 calculated with the full Floquet formulation and with $k_x, k_y = 0$. In the left panel, the original value of m_0 is negative and there are two Dirac points. As we increase the amplitude of the external field with right circular polarization $\eta = 1$ and $\hbar\Omega = 0.5$ eV, the Dirac points separate and even double, for $\mathcal{A} = 0.1, 0.2$ Å^{-1} there are four Dirac points. For $\mathcal{A} = 0.3$ Å^{-1} the four Dirac points have disappeared and gaps have opened in symmetric positions around the origin. For $\mathcal{A} = 0.5$ Å^{-1} the two Dirac points reappear. In the right panel we show the case with positive value of m_0 and how the Dirac points are switched on and off again as we increase $\mathcal{A}$. If we would have $\eta = -1$, the Dirac points would get closer to each other and to the origin as we increase $\mathcal{A}$, until they cancel each other at the origin and a gap opens. Note that the same band structure, including the Dirac nodes, is repeated periodically as a function of the quasi-energy with period $\hbar\Omega$. Also further nodes appear at higher values of $|k_z|$ (not shown in the figure) corresponding to band crossings with Floquet indices $|n| > 1$.

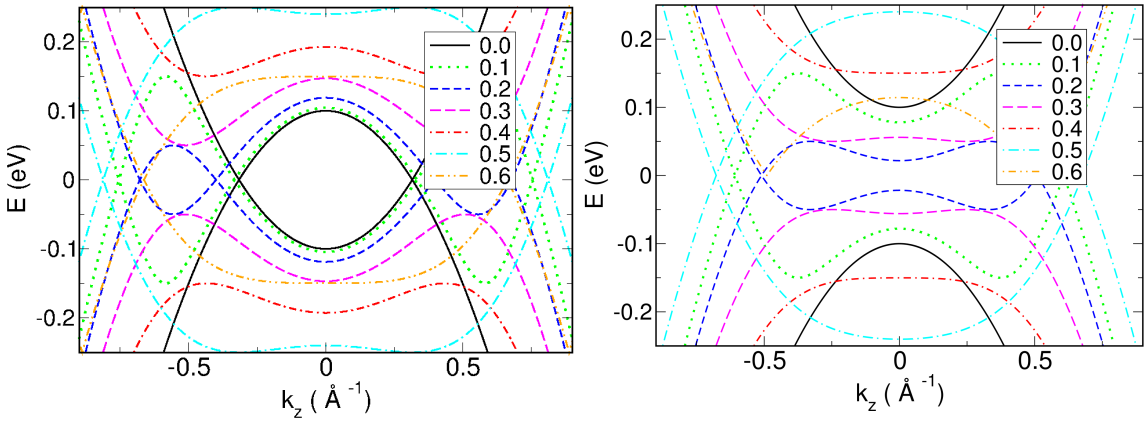

FIG. 5. Band structure in the first Floquet-Brillouin zone as a function of k_z with $k_x = k_y = 0$. The Hamiltonian parameters are $c_0 = c_1 = c_2 = 0.0, m_0 = -0.1$ eV (left) $m_0 = 0.1$ eV (right), $m_1 = m_2 = 1.0$ eV Å^2, $\hbar v = 1.0$ eV Å, $\zeta = 1$, and the external field parameters $\eta = 1$, $\hbar\Omega = 0.5$ eV, and several values of $\mathcal{A}$ indicated in the legend from 0.0 to 0.6 Å^{-1}. In the figure we have eliminated contributions from higher bands at large values of k_z for clarity of presentation.

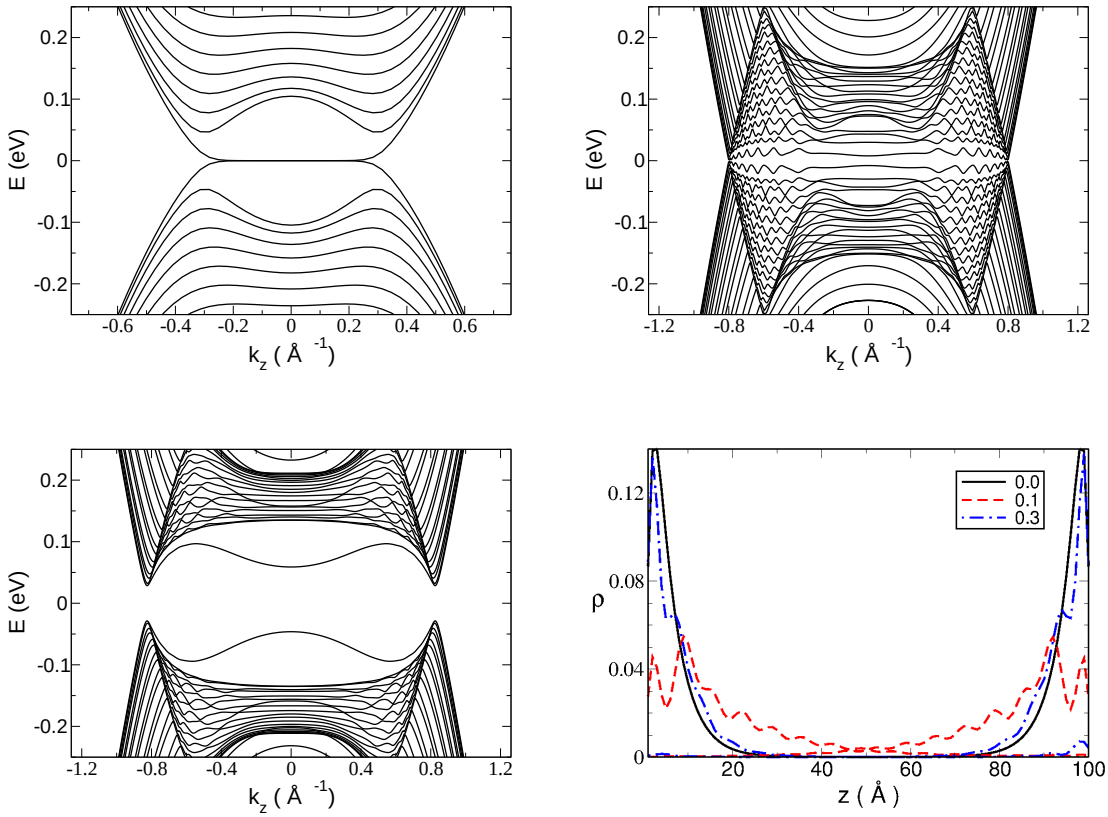

FIG. 6. Band structure for a slab of width $W = 100$ Å in the x direction and infinite in both the y and the z direction as a function of k_z and with $k_y = 0$. The Hamiltonian parameters are $c_0 = c_1 = c_2 = 0.0$, $m_0 = -0.1$ eV , $m_1 = m_2 = 1.0$ eV Å^2, $\hbar v = 1.0$ eV Å, $\zeta = 1$, and the external field parameters $\eta = 1$, $\hbar\Omega = 0.5$ eV, and $\mathcal{A} = 0.0$ (top left), 0.1 Å^{-1} (top right), 0.3 Å^{-1} (bottom left). In the right bottom plot, total electron density for states with $k_z = 0$ for the different values of $\mathcal{A}$ showing the exponential decay from the surface.

Results for a finite slab

To explore the evolution of the midgap Fermi arc states as the external field is switched on, we perform calculations in a slab of material with finite width W in the x direction but infinite in the y and z directions. We discretize the model Hamiltonian with a standard tight-binding regularization including the Floquet subbands. To make the analysis of the results easier, we present calculations including only one-photon processes, an approximation valid for small values of $\mathcal{A}$ and small values of k_z. A more complete analysis of the Full Floquet results is outside the scope of this work and will be presented elsewhere. In Fig. 6 we show different results of the band structure for a slab of material with the same parameters as the left panel of Fig. 5 with $\mathcal{A} = 0.0, 0.1, 0.3$ Å^{-1}. We see a band structure resembling the bulk bands calculated previously with midgap states in between the Dirac points. When there is no field, the midgap states form the Fermi arc typical of Weyl semimetals. States in the Fermi arc are surface states as shown in the right bottom panel of the figure. Without external field, there are two degenerate Fermi arc surface states, one in each surface. When the field is switched on but we still keep the Dirac points, the Fermi arc states loose the degeneracy between the different surfaces (case with $\mathcal{A} = 0.1$ Å^{-1}). For higher fields, when a gap is opened in the Dirac cones, the surface states are not topologically protected anymore (bottom left panel with $\mathcal{A} = 0.3$ Å^{-1}). In the bottom left panel we show the total electronic density as a function of the x coordinate for the states with $k_z = 0$ for the three values of $\mathcal{A}$ shown previously. There is an exponential decay of the surface states in the Fermi arcs when there is no field and similarly for small values of the field $\mathcal{A} = 0.1$ Å^{-1}. For larger fields $\mathcal{A} = 0.3$ Å^{-1}, the spatial decay from the surface is very much reduced as the gap is opened in the Dirac cones and the topological protection lost.

Signatures of the exceptional points in the complex plane k_z

As mentioned in the main text, the exceptional points in the spectrum of the Hamiltonian $\widetilde{H}_W$ come in complex conjugate pairs $k_i, \overline{k}_i$ in the complex plane of the momentum k_z. It may be actually seen that the lowest eigenvalue ε has along the line connecting each of these pairs the complex structure

$$\varepsilon(k_z) \sim \sqrt{k_i - k_z}\sqrt{\overline{k}_i - k_z} \tag{22}$$

The square root behavior means that k_i and $\overline{k}_i$ are branch points and that, for each pair, there are two different branches of the Riemann sheet going across the real axis of the complex plane. If we take for instance the line $\mathrm{Re}(k_z) = \mathrm{Re}(k_i)$, we get from (22)

$$\begin{aligned}\varepsilon(\mathrm{Re}(k_i) + iy) &\sim \sqrt{i\mathrm{Im}(k_i) - iy}\sqrt{-i\mathrm{Im}(k_i) - iy} \\ &= \sqrt{(\mathrm{Im}(k_i))^2 - y^2}\end{aligned} \tag{23}$$

This implies that there must be a segment of points connecting k_i and $\overline{k}_i$ (corresponding to $|y| < |\mathrm{Im}(k_i)|$) where the eigenvalue ε becomes purely real, with two possible opposite values from the two branches in the complex plane. On the other hand, when $|\mathrm{Im}(k_z)| > |\mathrm{Im}(k_i)|$, the above expression also implies the existence of a tail starting from k_i (and another from $\overline{k}_i$) where the real part of ε vanishes, while the imaginary part gets opposite values in the two different branches.

These features can be observed in the results obtained for the lowest eigenvalue ε after numerical diagonalization of the Hamiltonian, showing the existence of the branch cuts in the spectrum. We have represented for instance in Fig. 7 the absolute values of the real and imaginary parts of the eigenvalue ε for radiation parameters $\hbar\Omega = 0.1$ eV, $\mathcal{A} = 0.05\, a^{-1}$, and radius $R = 100a$ (a standing for a microscopic length scale in the material). One can clearly observe the signatures of four pairs of exceptional points for $\mathrm{Re}(k_z) > 0$, which follow to a good approximation the behavior expected from (22).

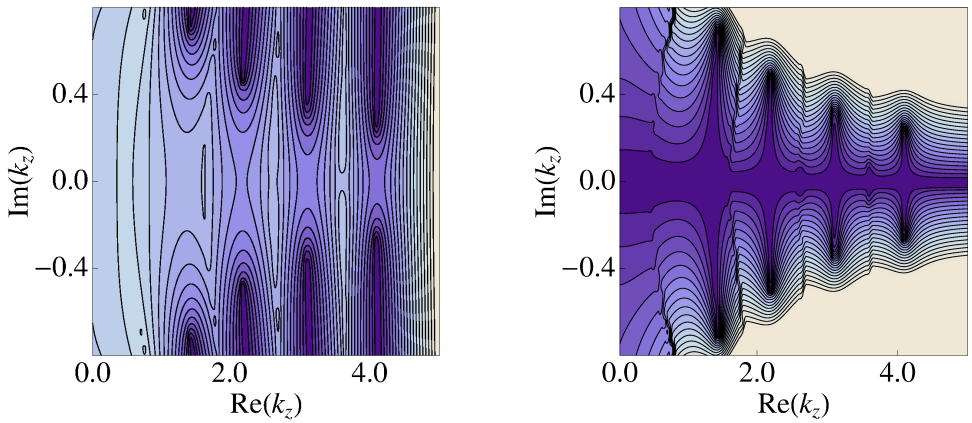

FIG. 7. Contour plots of the absolute values of the real part (left) and the imaginary part (right) of the lowest eigenvalue ε as a function of the momentum k_z in the complex plane, from values close to zero drawn in dark blue and larger absolute values shown in light blue. The parameters taken for the radiation are $\hbar\Omega = 0.1$ eV, $\mathcal{A} = 0.05\, a^{-1}$, and the radius of the cylindrical geometry considered in the main text is $R = 100a$ (where a stands for a typical microscopic length scale in the material).

As pointed out in the main text, the number of exceptional points grows linearly with the amplitude $\mathcal{A}$ of the vector potential as well as with the area of the surface exposed to the radiation. It can be seen in any case that each pair of complex conjugate exceptional points is tied to the same kind of complex structure, which guarantees their robustness as no small perturbation can unfold the topology of the underlying Riemann surface.

Evaluation of the angular component of the current and time evolution of the probability density

We review here the way in which the probability current $\mathbf{j}$ of the evanescent states can be computed from the spinor representation χ defined in the main text. The formal expression of the current $\mathbf{j}$ can be found multiplying first the

evolution equation by the complex conjugate of the original Weyl spinor ψ, which leads to

$$i\psi^\dagger \partial_t \psi = \psi^\dagger [-iv\sigma_x \partial_x - iv\sigma_y \partial_y - iv_z \sigma_z \partial_z + v\mathcal{A}\left(\sigma_x \cos(\Omega t) + \sigma_y \sin(\Omega t)\right)]\psi \tag{24}$$

We can take then the complex conjugate of (24), summing the pair of expressions thus obtained to end up with the continuity equation

$$\partial_t \left(\psi^\dagger \psi\right) + v\partial_x \left(\psi^\dagger \sigma_x \psi\right) + v\partial_y \left(\psi^\dagger \sigma_y \psi\right) + v_z \partial_z \left(\psi^\dagger \sigma_z \psi\right) = 0 \tag{25}$$

From this expression, we can read the current vector in cartesian coordinates

$$\mathbf{j} = (v\psi^\dagger \sigma_x \psi, v\psi^\dagger \sigma_y \psi, v_z \psi^\dagger \sigma_z \psi) \tag{26}$$

We are interested in particular in the angular component of the current (26), since we want to compute it for the evanescent states which are confined to circular rings on the surface exposed to the radiation. Passing to polar coordinates (r, θ), this angular component turns out to be

$$j^\theta = -\frac{\sin(\theta)}{r} v\psi^\dagger \sigma_x \psi + \frac{\cos(\theta)}{r} v\psi^\dagger \sigma_y \psi \tag{27}$$

Our goal is to compute j^θ from the expression of the eigenstates obtained in the spinor representation χ. To perform this operation, we must bear in mind that the spinors χ are related to the original Weyl fermions ψ by the consecutive action of the unitary transformations U and P defined in the main text, so that

$$\psi = e^{-i\left(-i\partial_\theta + \frac{1}{2}\sigma_z\right)\Omega t}\ e^{-i\mathcal{A}r\cos(\theta)}\ \chi \tag{28}$$

For the sake of facilitating the analytic evaluation of the current, we may assume at this point the condition $\mathcal{A}r \ll 1$. We get then

$$\begin{aligned}
j^\theta &= -\frac{\sin(\theta)}{r} v \left(e^{-\Omega t\partial_\theta}\chi^\dagger\right) e^{i\frac{1}{2}\sigma_z \Omega t} \sigma_x e^{-i\frac{1}{2}\sigma_z \Omega t} \left(e^{-\Omega t\partial_\theta}\chi\right) \\
&\quad + \frac{\cos(\theta)}{r} v \left(e^{-\Omega t\partial_\theta}\chi^\dagger\right) e^{i\frac{1}{2}\sigma_z \Omega t} \sigma_y e^{-i\frac{1}{2}\sigma_z \Omega t} \left(e^{-\Omega t\partial_\theta}\chi\right) \\
&= -\frac{\sin(\theta)}{r} v \left(e^{-\Omega t\partial_\theta}\chi^\dagger\right) \left(\sigma_x \cos(\Omega t) - \sigma_y \sin(\Omega t)\right) \left(e^{-\Omega t\partial_\theta}\chi\right) \\
&\quad + \frac{\cos(\theta)}{r} v \left(e^{-\Omega t\partial_\theta}\chi^\dagger\right) \left(\sigma_x \sin(\Omega t) + \sigma_y \cos(\Omega t)\right) \left(e^{-\Omega t\partial_\theta}\chi\right) \\
&= -i\frac{v}{r}\left(e^{-i(\theta-\Omega t)} \left(e^{-\Omega t\partial_\theta}\chi_1^*\right) \left(e^{-\Omega t\partial_\theta}\chi_2\right) - e^{i(\theta-\Omega t)} \left(e^{-\Omega t\partial_\theta}\chi_2^*\right) \left(e^{-\Omega t\partial_\theta}\chi_1\right)\right)
\end{aligned} \tag{29}$$

We may now work out the expression of the current for a spinor χ representing the hybridization between states with projection of the total angular momentum $j_z = \hbar/2$ and $-\hbar/2$ (omitting at this point the common k_z-dependence for simplicity)

$$\chi \sim \begin{pmatrix} \phi_1(r) \\ e^{i\theta}\phi_2(r) \end{pmatrix} + \begin{pmatrix} e^{-i\theta}\phi_3(r) \\ \phi_4(r) \end{pmatrix} \tag{30}$$

It can be seen that, if we compute j^θ for each spinor contribution with well-defined j, the periodic time dependence is canceled out in the expression (29). If instead we carry out the full calculation allowing for the mixing of the two spinor contributions, we get a piece in j^θ that keeps the periodic time dependence as in Eq. (29). We obtain the result

$$j^\theta = j^\theta_{\text{static}} + j^\theta_\Omega \tag{31}$$

with

$$j^\theta_{\text{static}} = -i\frac{v}{r}(\phi_1^*\phi_2 - \phi_2^*\phi_1 + \phi_3^*\phi_4 - \phi_4^*\phi_3) \tag{32}$$

and

$$j^\theta_\Omega = -i\frac{v}{r}(e^{-i(\theta-\Omega t)}\phi_1^*\phi_4 - e^{i(\theta-\Omega t)}\phi_4^*\phi_1 + e^{i(\theta-\Omega t)}\phi_3^*\phi_2 - e^{-i(\theta-\Omega t)}\phi_2^*\phi_3) \tag{33}$$

The static component $j^{\theta}_{\rm static}$ is made of the contributions from the two spinors with $j_z = \hbar/2$ and $j_z = -\hbar/2$, which tend to cancel each other when integrating the current to obtain the intensity across the radial direction. The two different contributions are represented for instance in Fig. 8 for a typical evanescent state at the outermost region of the surface exposed to the radiation. The cancellation operating in the integral $\int dr\, r j^{\theta}_{\rm static}$ leads in general to rather small values of the intensity associated to $j^{\theta}_{\rm static}$. This does not apply however to the time-dependent component j^{θ}_{Ω}, as shown in Fig. 8. The intensity obtained from this current turns out to have maxima (in the angular variable) that are about two orders of magnitude larger than that from $j^{\theta}_{\rm static}$, providing then the main observable signal of the evanescent states.

We can express the time-dependent component as

$$j^{\theta}_{\Omega}(r,\theta) = \frac{v}{r} f(r, \theta - \Omega t) \tag{34}$$

in terms of a function with the periodicity $f(r, \theta + 2\pi) = f(r,\theta)$. The continuity equation can be approximated then by

$$\begin{aligned} \partial_t \left(\psi^{\dagger}\psi\right) &\approx -\partial_{\theta} j^{\theta}_{\Omega} \\ &= -\frac{v}{r}\partial_{\theta} f(r, \theta - \Omega t) \end{aligned} \tag{35}$$

Eq. (35) can be integrated at once to give

$$\psi^{\dagger}\psi \approx \frac{v}{\Omega r} f(r, \theta - \Omega t) + \text{const.} \tag{36}$$

This shows that the probability density of the evanescent states has a time evolution that is inherited from the time dependence of the current.

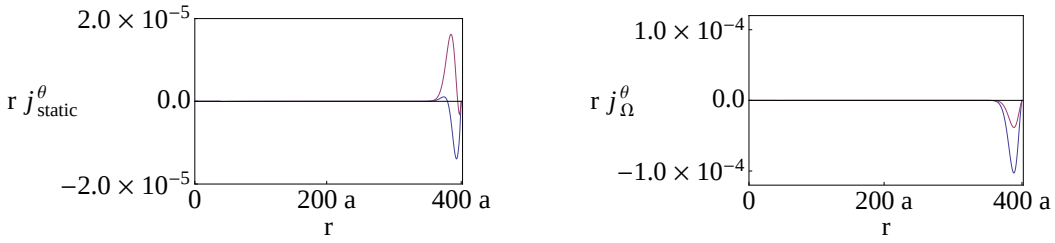

FIG. 8. Left: Plot of the two contributions to $r j^{\theta}_{\rm static}$ (in units of v/a^2, where a stands for a microscopic length scale in the material) from the spinors with $j_z = \hbar/2$ (blue) and $j_z = -\hbar/2$ (red) making up the evanescent state represented at the top of the left panel in Fig. 4 of the main text. Right: Plot of the two contributions to $r j^{\theta}_{\Omega}$ at $t = 0$, $\theta = 0$ (in units of v/a^2) from the first two terms (blue) and the last two terms (red) in Eq. (33), for the same state as in the left plot. The parameters of the radiation are $\hbar\Omega = 0.5$ eV, $\mathcal{A} = 0.005\, a^{-1}$, and the corresponding radius of the cylindrical geometry is $R = 400a$.

Similar results are obtained when considering the evanescent states from the hybridization of bands with values of the projection of the total angular momentum differing by two units of $\hbar$. This case is relevant since it corresponds to the appearance of evanescent states with quasi-energy $\epsilon = 0$ in the conventional Floquet approach. We may start for instance with a linear combination of states with $j_z = \hbar/2, -\hbar/2$ and $-3\hbar/2$

$$\chi \sim \begin{pmatrix} \phi_1(r) \\ e^{i\theta}\phi_2(r) \end{pmatrix} + \begin{pmatrix} e^{-i\theta}\phi_3(r) \\ \phi_4(r) \end{pmatrix} + \begin{pmatrix} e^{-2i\theta}\phi_5(r) \\ e^{-i\theta}\phi_6(r) \end{pmatrix} \tag{37}$$

Inserting (37) into (29), we observe that the angular current can be decomposed now into three different contributions

$$j^{\theta} = j^{\theta}_{\rm static} + j^{\theta}_{\Omega} + j^{\theta}_{2\Omega} \tag{38}$$

with

$$j^{\theta}_{\rm static} = -i\frac{v}{r}(\phi_1^*\phi_2 + \phi_3^*\phi_4 + \phi_5^*\phi_6) + \text{h.c.} \tag{39}$$

$$j^{\theta}_{\Omega} = -i\frac{v}{r}(e^{-i(\theta-\Omega t)}\phi_1^*\phi_4 + e^{i(\theta-\Omega t)}\phi_3^*\phi_2 + e^{-i(\theta-\Omega t)}\phi_3^*\phi_6 + e^{i(\theta-\Omega t)}\phi_5^*\phi_4) + \text{h.c.} \tag{40}$$

$$j^{\theta}_{2\Omega} = -i\frac{v}{r}(e^{-2i(\theta-\Omega t)}\phi_1^*\phi_6 + e^{2i(\theta-\Omega t)}\phi_5^*\phi_2) + \text{h.c.} \tag{41}$$

As shown with the Floquet approach in the main text, the hybridization of the bands differing by two units of $\hbar$ in the projection of the total angular momentum (energy difference equal to $2\hbar\Omega$) opens a gap along a circle in momentum space. It can be seen that the resulting evanescent states are confined in concentric circular rings on the surface exposed to the radiation, with currents $j^{\theta}_{\rm static}$ and j^{θ}_{Ω} which have very small intensities when integrated along the radial direction. However, the component $j^{\theta}_{2\Omega}$ leads to maxima of the intensity (in the angular variable) which are about two orders of magnitude larger than those from $j^{\theta}_{\rm static}$ and j^{θ}_{Ω}, producing a significant modulation of the charge which rotates with frequency Ω. In this case we have

$$j^{\theta}_{2\Omega}(r,\theta) = \frac{v}{r} g(r, \theta - \Omega t) \tag{42}$$

in terms of a periodic function with $g(r, \theta + \pi) = g(r, \theta)$. The probability density of the evanescent states has now a time evolution given by

$$\psi^{\dagger}\psi \approx \frac{v}{\Omega r} g(r, \theta - \Omega t) + \text{const.} \tag{43}$$

From (36) and (43), we actually conclude that the charge of the evanescent states must have an angular modulation and that, moreover, it has to rotate with the same frequency Ω of the radiation, along the rings where the states are confined.